10 Aug 2016

Modal Response as a Validation Technique for Metal Parts Fabricated with Selective Laser Melting

Joshua D. Pribe

Brian M. West

Michelle L. Gegel

Troy Hartwig

et. al. For a complete list of authors, see https://scholarsmine.mst.edu/mec_aereng_facwork/4397

Recommended Citation

J. D. Pribe et al., "Modal Response as a Validation Technique for Metal Parts Fabricated with Selective Laser Melting," *Proceedings of the 27th Annual International Solid Freeform Fabrication Symposium (2016, Austin, TX)*, pp. 151-174, University of Texas at Austin, Aug 2016.

Solid Freeform Fabrication 2016: Proceedings of the 27th Annual International Solid Freeform Fabrication Symposium – An Additive Manufacturing Conference
Reviewed Paper

MODAL RESPONSE AS A VALIDATION TECHNIQUE FOR METAL PARTS FABRICATED WITH SELECTIVE LASER MELTING

Joshua D. Pribe*, Brian M. West*, Michelle L. Gegel*, Troy Hartwig†, Toby Lunn†, Ben Brown†, Douglas A. Bristow*, Robert G. Landers*, Edward C. Kinzel*

*Department of Mechanical and Aerospace Engineering, Missouri University of Science and Technology, Rolla, MO 65409
†Department of Energy's Kansas City National Security Campus Managed by Honeywell FM&T, Kansas City, MO 64147

Abstract

This paper investigates modal analysis as a validation technique for additively manufactured parts. The Frequency Response Function (FRF) is dependent on both the geometry and the material properties of the part as well as the presence of any defects. This allows the FRF to serve as a "fingerprint" for a given part of given quality. Once established, the FRF can be used to qualify subsequently printed parts. This approach is particularly attractive for metal parts, due to the lower damping as well as use in high-value applications where failure is unacceptable. To evaluate the efficacy of the technique, tensile specimens are printed with a Renishaw AM250, the modal response of these parts is characterized prior to tensile testing, and the FRFs are compared to their engineering metrics for parts printed with both nominal and off-nominal parameters. Numerical modeling is used to understand the modal structure, and the possibility of defect prognosis is also explored by comparing the measured response to simulation results.

Introduction

The field of metal Additive Manufacturing (AM) has seen rapid growth over the past several years. The AM process is especially well suited for components with low production volumes and expensive materials or geometries that would otherwise require costly machining processes. However, the wide variety of processing parameters inherent in AM techniques makes it difficult to create standard qualification methods for AM components [1]. This has slowed its widespread adoption in industries like aerospace that require consistently reliable parts [2].

Much of the literature addressing this challenge focuses on nondestructive testing (NDT) to detect defects and relate them to processing parameters. These defects include hollow or missing particles that introduce porosity, contamination by oxygen or nitrogen remaining in the build chamber, and undesired residual stresses arising as the part solidifies [3]. Particular attention has been given to porosity detection, with computed tomography (CT) as the dominant technique [4]. CT scans allow microstructure to be visualized and the percent density to be computed.

In several studies, CT scans on metal AM parts have been used to determine the effect of parameters like sample orientation, sample geometry, and hatching strategy on the existence, shape, and size of porosity [5-7]. Ultrasonic sensing has also been proposed as an in-situ technique for monitoring porosity evolution during a build and providing feedback control [8-9]. This strategy is limited by the sensitivity of ultrasonic measurements to surface roughness [9].

Other studies have investigated the mechanical properties of AM parts through destructive tests. For example, Wang et al. [10] linked laser power and scanning speed with yield and ultimate strengths of AM stainless steel specimens. They also noted AM specimens of the same material showed a wide range of strengths and percent elongations depending on the overall combination of processing parameters used in a given study. Everhart et al. [11] considered the effect of surface roughness and post-build machining on the yield and ultimate strengths of AM specimens.

NDE techniques based on modal analysis are well documented for large-scale civil and mechanical applications, typically in the field of structural health monitoring [12-13]. Modal testing has also been applied to individual components, often through measuring a part's response to a hammer impact test. Generally, changes in material properties will in turn affect a part's modal parameters, which can be detected in vibration tests. One method, for example, was developed to test sprockets made using powder metallurgy as a "go/no go" test just prior to shipment [14]. Finite element models also have been investigated as a way to identify the correct mode shapes for experimentally measured natural frequencies [15]. This was demonstrated by creating a finite element model from CT scan data for cast automotive steering knuckles. The simulated natural frequencies fairly closely matched experimental measurements. The simulated mode shapes could then be used to help determine the locations of defects that shifted certain natural frequencies.

In one recent study, Schoneman and Allen [16] performed roving hammer tests on two direct metal laser sintered components made from Ti6Al4V and Inconel 718, respectively. Assuming that the natural frequencies of the components were proportional to the square root of the stiffness to density ratio, measured modes and densities of the parts were used to optimize the stiffness value in a finite element model. This updated stiffness closely matched the results for the Inconel 718 component, but the results were less conclusive for the Ti6Al4V component. The authors indicated that there may have been some effects from anisotropy in the latter component.

In this paper, we seek to study the links between build parameters and frequency response (modal analysis) results and between frequency response and the actual mechanical properties of the component. We propose modal analysis as an efficient way to rapidly evaluate large numbers of parts. To facilitate this goal, we test the parts as printed on the build plate. This introduces some complexity in the modal response due to coupling between the parts but eliminates the need for fixturing. This allows quick testing of large numbers of parts, especially compared to CT scanning. Modal analysis results for each part can be correlated with the part's mechanical properties, including Young's modulus, yield strength, and ultimate strength, determined through destructive tests. The empirical measurement of density and Young's modulus can be used to improve the fidelity of finite element modal simulations. (Patent Pending Application Number 14/941,258)

Materials and Test Specimens

In this study, a Renishaw AM 250 was used to fabricate a series of rectangular tensile test specimens using selective laser melting (SLM) of 304L stainless steel. The SLM process involves layer-by-layer fusion of powder particles by heating with a laser. The laser heats the powder bed point-by-point. After scanning a layer with the laser, the build platform is lowered and a new layer of powder (50 μm thick) is coated over the entire build. Fully melting the powder creates parts that can be nearly 100% dense [2].

In the experiments described in this paper, two build plates of tensile test specimens were fabricated. One of the builds had specimens with uniform process parameters and the second included specimens with intentionally varied laser power. The set of specimens on each build plate was excited with an electrodynamic shaker, and the vibration response was measured using a Laser Doppler Vibrometer (LDV). Density measurements and tensile tests were then performed on each specimen, with some of them machined to the ASTM E8 standard [17]. By correlating the modal analysis with the mechanical properties of AM parts, modal analysis can be used as a validation technique.

The design of the tensile test specimens was based on the subsize rectangular specimen in ASTM E8 [17]. Each outside dimension was approximately 0.05 in. larger than the dimensions given in the standard. The build plates (referred to as Builds 1 and 2) each contained a combination of specimens with three different geometries, shown in Fig. 1a. Fig. 1b shows a photograph of a plate during vibration testing.

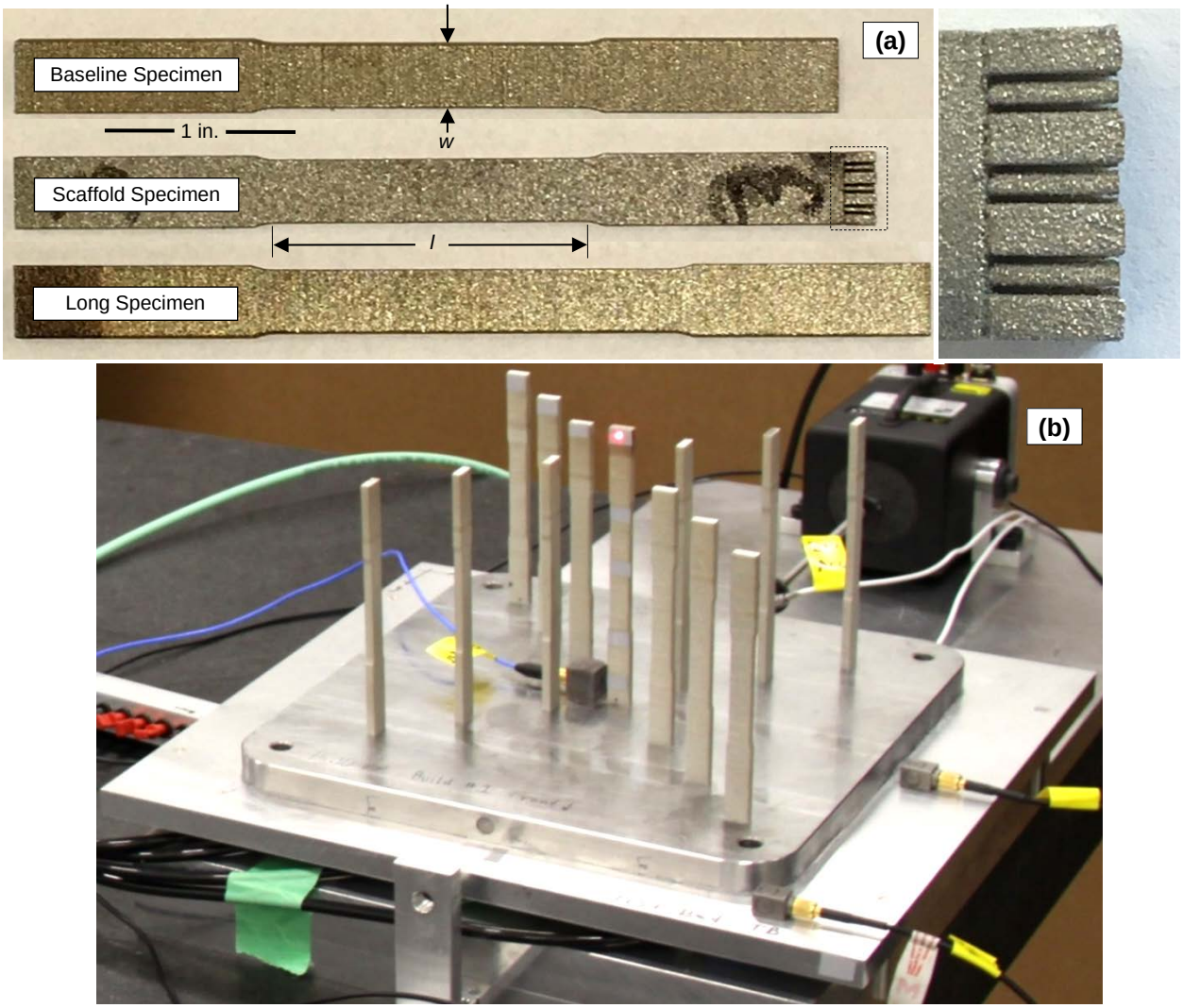

Fig. 1. (a) Tensile specimens with expanded view of scaffold. (b) Photograph of a build plate on the shaker table.

Each Baseline Specimen had a reduced section length of l=1.75 in. (44.45 mm), gauge width of w=0.35 in. (8.89 mm), and thickness of 0.15 in. (3.81 mm). The length and thickness were chosen based on modal simulations to have as many modes as possible between about 150 and 2000 Hz, the useful range of the LDV.

Each Scaffold Specimen was identical to the Baseline Specimen but with a support structure between the specimen and build plate. The scaffold is typical of AM builds and serves to isolate these specimens from coupling with the modes of other specimens in vibration testing.

Finally, each Long Specimen was identical to the Baseline Specimen but with a reduced section length of 2.25 in. (57.15 mm). One Long Specimen was included in the center of each build plate to analyze the effect of a specimen with a clearly lower set of natural frequencies.

Several specimens were also machined to the ASTM E8 standard after vibration testing and removal from the plate. Post-machining, the specimens had a thickness of 0.1 in. (2.54 mm) and a gauge width of 0.25 in. (6.35 mm), shown in Fig. 2.

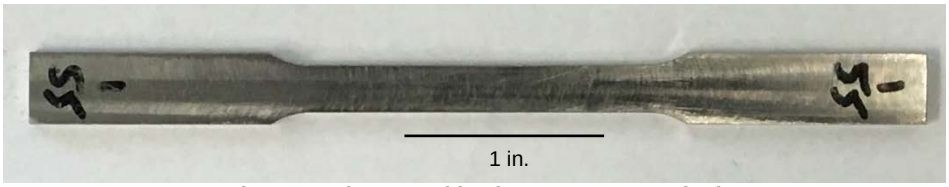

Fig. 2. Specimen machined to ASTM E8 standard

The specimens in both builds were arranged as shown in Fig. 3. Names for each specimen location were created using the *x*-*y* coordinate system shown in the figure. The figure also shows the two different orientations specimens could be built in. These location and orientation descriptors will be used throughout the rest of this paper.

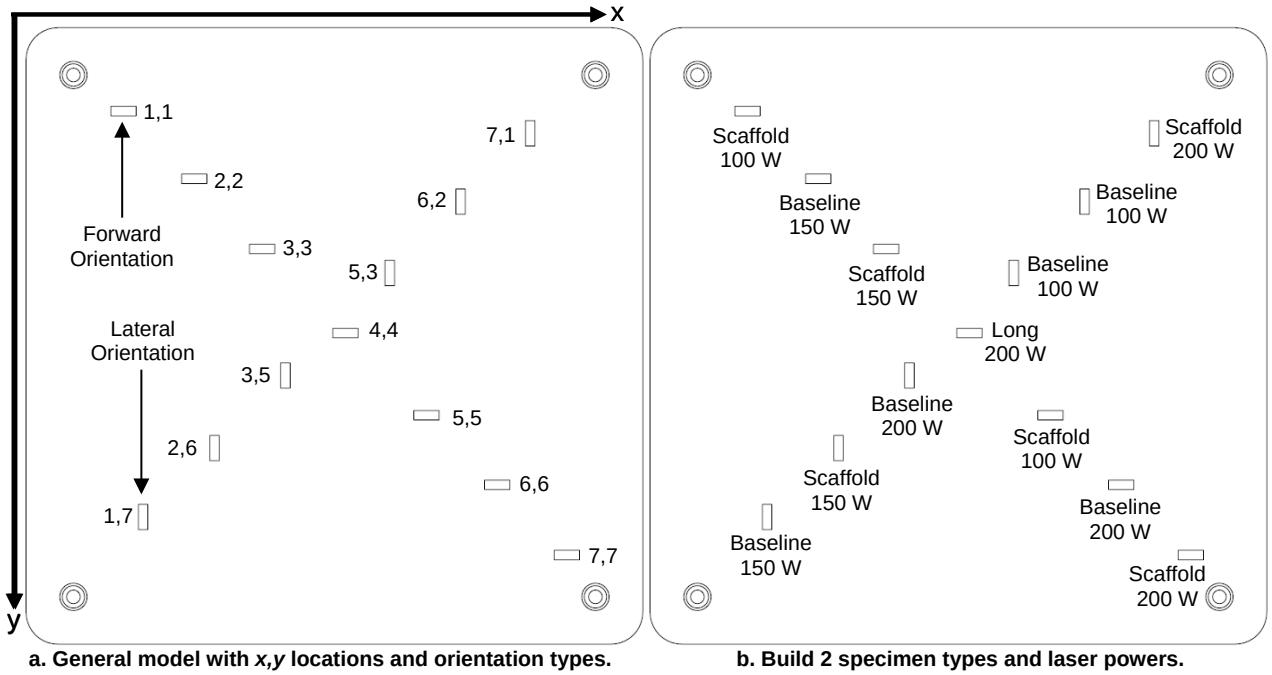

a. General model with *x,y* locations and orientation types. **b. Build 2 specimen types and laser powers.**

Fig. 3. Build plate models and specimen types and orientations.

The specimens were offset in the *x* and *y* directions so every specimen face could be line-of-sight accessed by the LDV during shaker tests. All specimens were built in the AM250 using 304L stainless steel, with 200 W laser power on Build 1 and varying laser powers on Build 2.

Modal Analysis Results

Frequency response function (FRF) measurements were taken using a shaker table for excitation. For each test, the build plate was excited in the *y* direction with a 20-2000 Hz sine chirp. An LDV recorded the response of a single specimen in the *x* or *y* direction. Tests were repeated until the LDV had recorded the response of every specimen in both directions. Post-test, the LMS PolyMAX technique was used to estimate modal parameters for each specimen.

The tests excited three bending modes of the specimens. The first and third modes were fore-aft bending modes, and the second mode was a side-to-side bending mode. Figure 4 shows the mode shapes for these modes, and Table 1 gives the approximate frequencies. The frequencies varied based on material and geometric properties. The direction of vibration for each mode was also dependent on a given specimen's orientation on the build plate, shown before in Fig. 3.

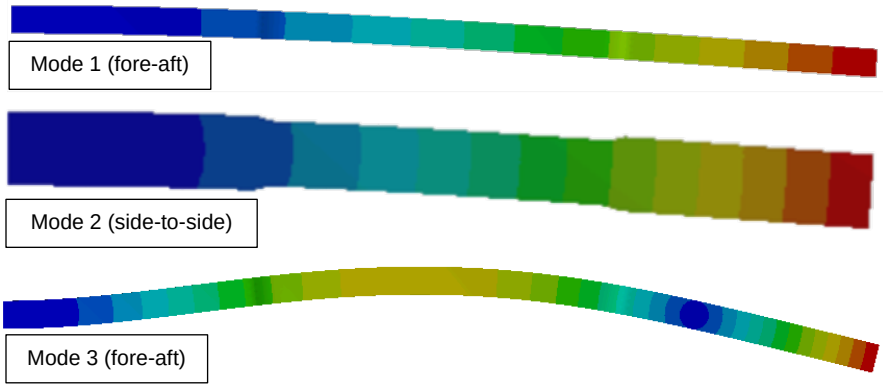

Fig. 4. Mode shapes of the three specimen bending modes measured in the modal tests.

Table 1. Modes and corresponding frequencies excited by the shaker table. The direction of vibration for the mode based on the specimen orientation is also included.

Mode	Mode Type	Approximate Frequency (Hz)	Direction of vibration for forward specimens	Direction of vibration for lateral specimens
1	Fore-aft	200	*y* direction	*x* direction
2	Side-to-side	500	*x* direction	*y* direction
3	Fore-aft	1250	*y* direction	*x* direction

Build 1 Results

Figure 5 shows the FRF for each specimen in Build 1, ordered by orientation. Since the build plate was nominally excited in the *y* direction, the *x*-direction response is the result of cross-axis motion in the slip table. This caused modes 1 and 3 to be excited for the lateral specimens and mode 2 to be excited for the forward specimens.

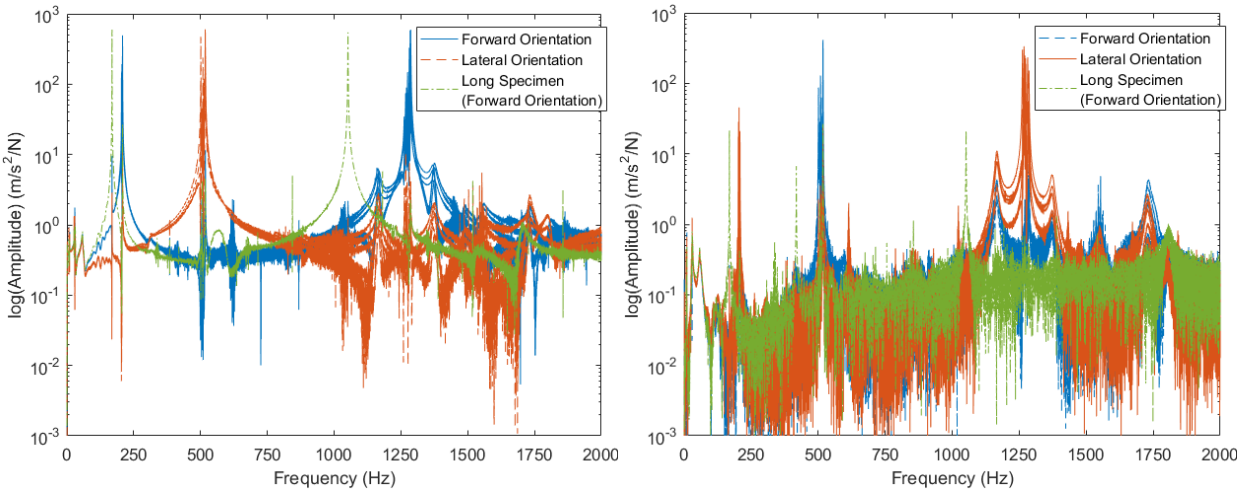

a. FRFs measured in *y* direction **b. FRFs Measured in *x* direction**

Fig. 5. FRFs of all Build 1 specimens, sorted by orientation.

The first mode appears near 200 Hz for all specimens. At this mode, the response of the forward specimens could be measured in the *y* direction while the response of the lateral specimens could be measured in the *x* direction. Figure 6 shows a close-up of this region from measurements in each direction. The dashed lines are at the natural frequencies identified by the modal analysis for each specimen.

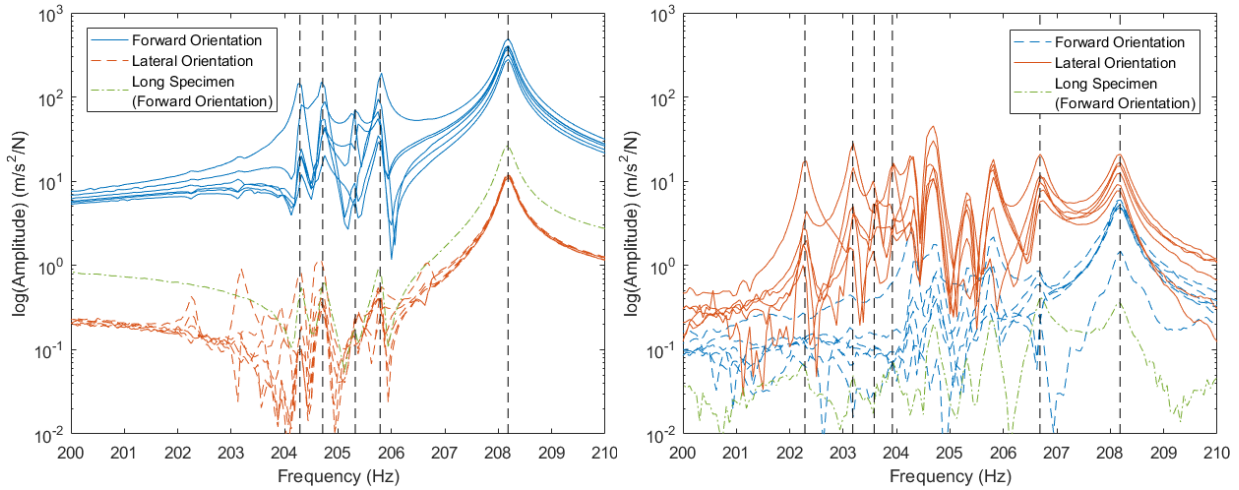

a. FRF measured in *y* direction, with dashed lines at forward specimen natural frequencies. **b. FRF measured in *x* direction, with dashed lines at lateral specimen natural frequencies.**

Fig. 6. FRFs of all Build 1 specimens at first mode.

Data from both directions indicates a dominant natural frequency for all specimens at 208.2 Hz, and the *x*-direction data shows another dominant frequency at 206.7 Hz for the lateral specimens. Some mode-splitting occurred as well, due most likely to a combination of out-of-phase vibrations and material and geometric property variations among the specimens. This produced several degenerate modes in the 202.2-205.8 Hz range for individual specimens or groups of specimens. Finally, the plots also show clear evidence of coupling. The Long Specimen, for instance, vibrates at the dominant mode of the rest of the forward specimens.

Again, the second and third modes appeared near 500 Hz and 1250 Hz, respectively. The FRFs around the second mode showed very similar behavior to the first mode, with two dominant frequencies and evidence of mode-splitting. The natural frequencies were somewhat more spread out at the third mode, likely because the effects of small geometry and material property changes become stronger at higher-order frequencies. Modes of the build plate also appeared on either side of 1250 Hz; these were identifiable through their higher damping. The dominant frequencies for modes 1 and 2 are shown in Table 2.

Table 2. Dominant frequencies at the first and second modes for Build 1 specimens.

Mode	Measurement Direction	Dominant Frequency (Hz)	Specimens
1	*y*	168.743	Long specimen
	x	206.683, 208.181	Lateral specimens
	y	208.181	Forward specimens
2	*x*	418.505	Long specimen
	y	517.707	Lateral Specimens
	x	518.286	Forward Specimens

Build 2 Results

Figure 7 shows the FRF for each specimen in Build 2 in each direction.

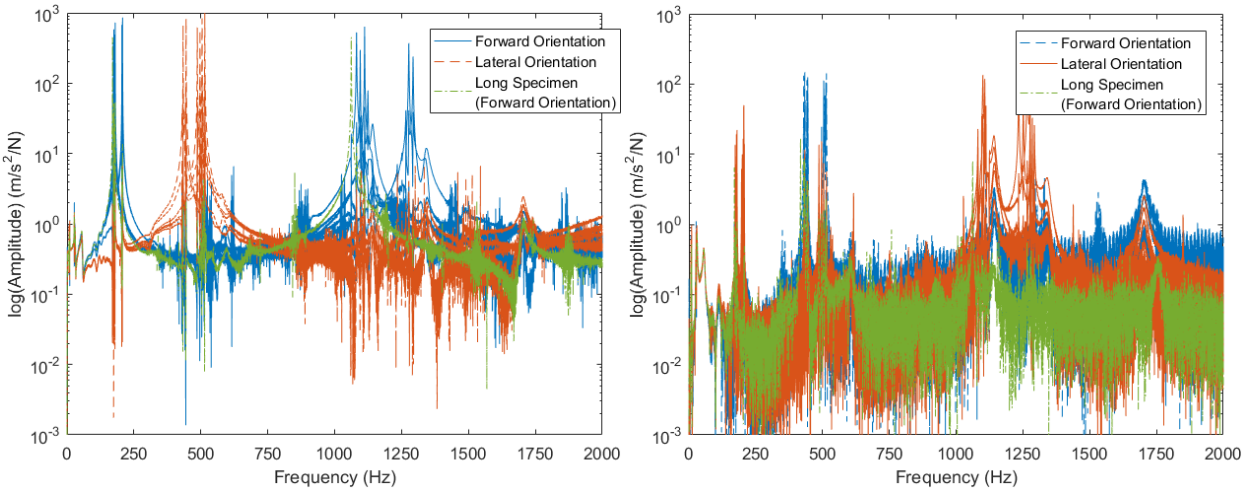

a. FRFs measured in *y* direction **b. FRFs measured in *x* direction.**

Fig. 7. FRFs of all Build 2 specimens, sorted by orientation.

In this case, there are two separate sets of peaks near each mode location. This is due to the presence of the longer Scaffold Specimens. The peaks within each set are also more spread out due to the property variations arising from the different laser powers. This allows a unique natural frequency to be identified for each specimen at each mode, without the single dominant frequency seen in Build 1. Figure 8 shows a close-up of the region near the first mode. The dashed lines are at the natural frequencies identified by the modal analysis for each specimen.

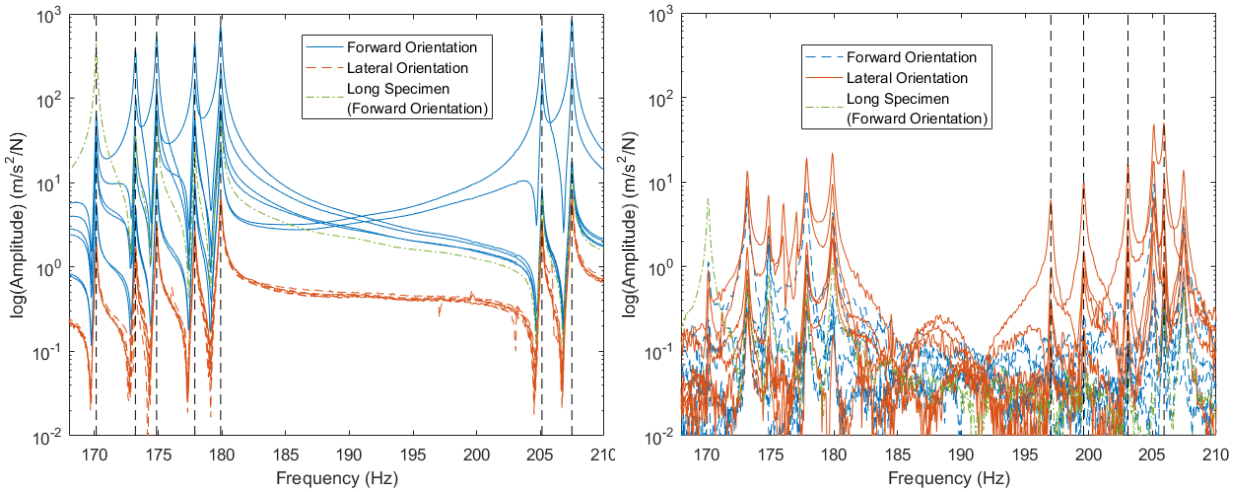

a. FRF measured in *y* direction, with dashed lines at forward specimen natural frequencies.

b. FRF measured in *x* direction, with dashed lines at lateral specimen natural frequencies.

Fig. 8. FRFs of all Build 2 specimens at first mode.

The modal analysis technique clearly identified the natural frequency for each of the forward specimens, shown by the dashed lines in Fig. 8a. It also identified the natural frequency for each of the lateral Baseline Specimens, shown by the dashed lines in Fig. 8b. However, the modal analysis did not identify a natural frequency for any of the lateral Scaffold Specimens. This would indicate that the scaffold may have reduced some of the effects of misalignment for these specimens. On the other hand, the modal analysis did identify the natural frequencies of all of the specimens at modes 2 and 3.

For the Build 2 results as a whole, the natural frequencies appeared to correlate well with the laser powers. This will be discussed further in relation to the tensile test results for each specimen. This allows the build power, modal results, and specimen strengths to be related, providing information on the viability of modal analysis as a validation technique.

Material Property Results

Density Measurements

Density measurements were performed using Archimedes' principle pursuant to ASTM B311 [20]. Using a scale with a precision of 0.001 g, all specimens were first weighed in air. Repeated measurements of each specimen in air differed by, at most, 0.001 g, indicating that the scale resolution was the main source of uncertainty. The specimens were then weighed in water three times. In this case, the standard deviation in the measurement for each specimen exceeded the resolution of the scale, so the standard deviation was used for the uncertainty bounds.

The results for Build 1, which used 200 W laser power, are summarized in Fig. 9, including error bounds based on the uncertainty sources described above. The Long Specimen (at location 4,4) was excluded because it was too long for any available beakers. The specimens at locations 7,1 and 7,7 appear to have lower densities, but the variance in the data for 7,7 in particular makes it difficult to tell if its density is actually significantly different from the others.

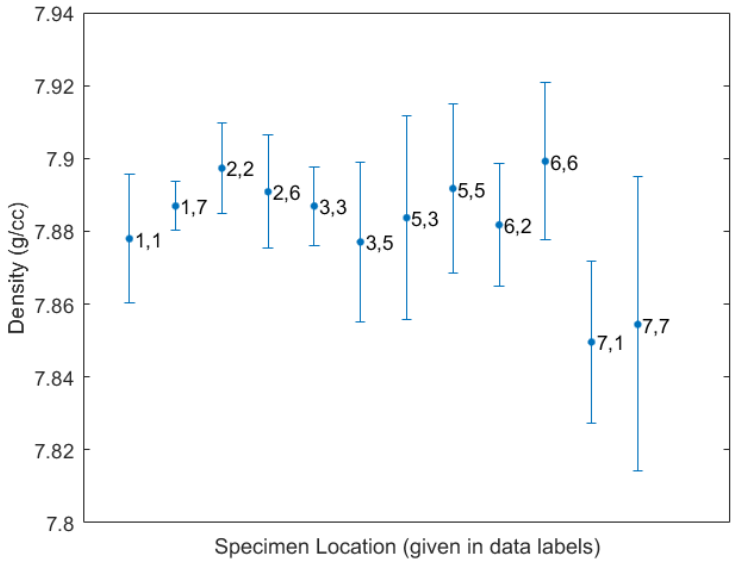

Fig. 9. Build 1 density results by specimen location.

The results for Build 2 are summarized in Fig. 10, again with error bounds. The average and standard deviation across all of the specimens in Build 1 are included for reference. The Long Specimen was again excluded. As opposed to the Baseline specimens, it was more difficult to ensure that the Scaffold Specimens were not touching the sides of the beaker and were free of air bubbles in the water. This typically led to larger variances in the measurement of their mass in water, reflected in the generally larger error bars for the Scaffold Specimens in the plot.

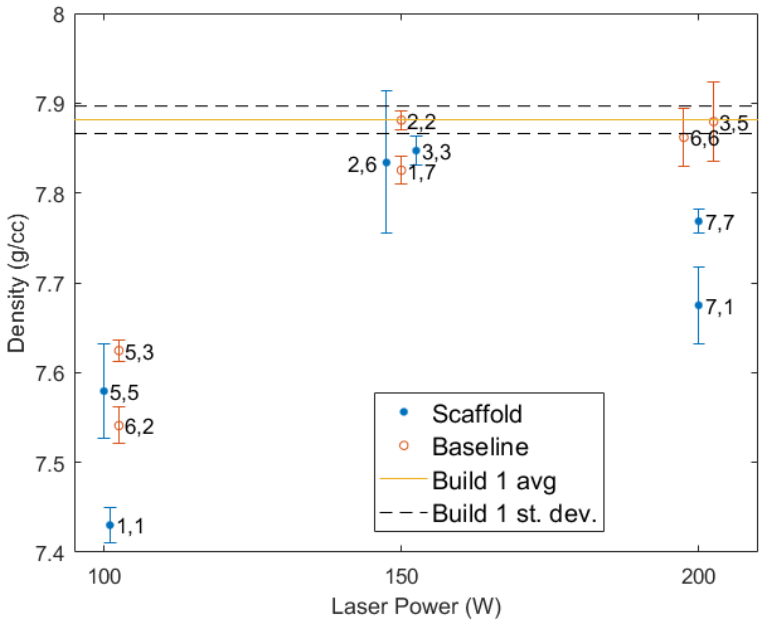

Fig. 10. Build 2 density results by specimen location, laser power, and type. Some specimens are slightly offset from 100 W, 150 W, and 200 W so that the error bars are visible.

The specimens built at 100 W were clearly less dense than the others. There was no clear difference between 150 W and 200 W specimens, with the exception of location 7,1 and, to a lesser

extent, 7,7. The specimen at 7,1 appeared to be much more porous than expected, given its 200 W laser power. The specimen at 7,7 was about 0.1 g/cc lower than expected.

One important note on the density testing is that surface-connected porosity, which causes a part to gain weight in water, can artificially raise the part's apparent density. Slotwinski et al. [8] observed this in AM cobalt-chrome parts. As a result, these density measurements are mostly useful for revealing large variations, such as the decrease in density for the 100 W specimens. It is more difficult to draw conclusions about, for instance, the specimen at 7,7, which deviated much less from the expected value based solely on Archimedes' method measurements.

CT scans were also performed on two Build 1 specimens (locations 1,7 and 7,7) and four Build 2 specimens (locations 1,7; 3,5; 6,2; and 7,7). This process determined their percent density based on the size of pores in the gauge section. The results are shown in Table 3.

Table 3. CT scanning results.

Build	Laser Power (W)	Specimen Location	Percent Density
1	200	1,7	99.468%
		7,7	99.779%
2	100	6,2	94.440%
	150	1,7	99.349%
	200	3,5	99.349%
		7,7	99.733%

This data generally supports the conclusion from the Archimedes' method tests: the 100 W specimens are clearly less dense, but the 150 W and 200 W specimens are comparable. This also indicates that the Archimedes' method measurement of the specimen at 7,7 is too low, possibly due to effects of the scaffold described previously.

Tensile Tests

Prior to tensile testing, the width and thickness at 3 points along the gauge length of each specimen were measured with a micrometer. These measurements were averaged to determine the cross sectional dimensions for stress calculations. An Instron UTM and Bluehill 3 software were used to conduct and record data from the tensile tests.

Each tensile test consisted of 10 cycles within the elastic region, followed immediately by pulling the specimen to fracture. The cycling allowed determination of Young's modulus per ASTM E111, which involves taking the average of the modulus calculated for each cycle [21]. The as-printed specimens were cycled between 10 and 60 MPa while the machined specimens were cycled between 25 and 75 MPa because there appeared to be some slack in the system at the lower stresses for those specimens. The rest of the test was done using the ASTM E8 procedure [17]. Representative data for the low-strain region is shown in Fig. 11 for each type of specimen that was tested.

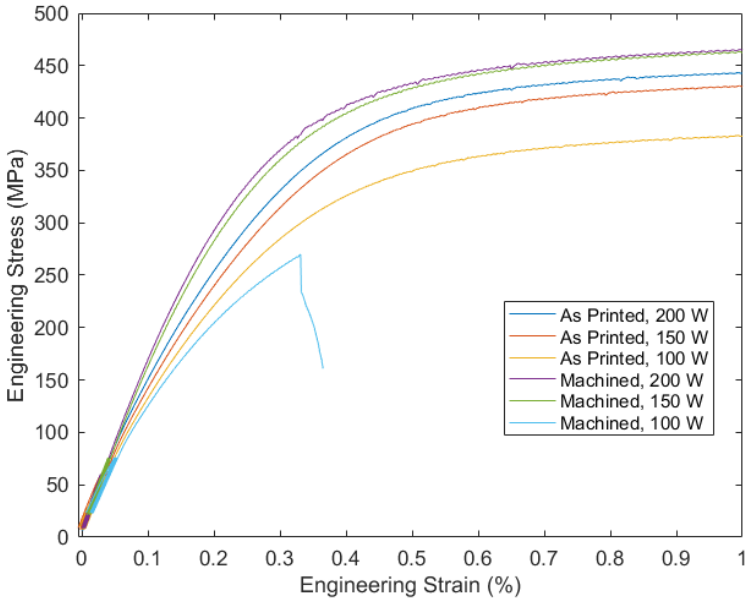

Fig. 11. Representative low-strain data for each laser power. The cycling at the beginning of the test is visible in the bottom left of the plot.

The machined 100 W specimen broke suddenly at 270.2 MPa at an apparent delamination. The as-printed 100 W specimen clearly yielded at a lower stress while the plots for the 150 W and 200 W as-printed specimens were closer to each other. Finally, the machined 150 W and 200 W specimens were extremely similar, with only a slight difference in yield strength.

Figure 12 shows representative data for a full tensile test. This includes an increase in strain rate at 2% strain, which is allowed under the standard after yielding has occurred [17].

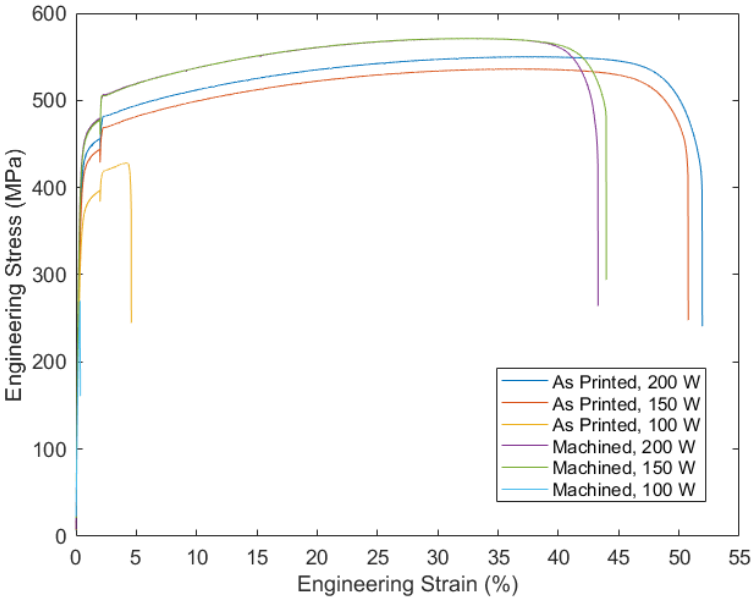

Fig. 12. Representative full tensile test data for each laser power.

The as-printed 100 W specimen was again clearly different from the others, as it broke suddenly at 428.2 MPa. The other two as-printed specimens were also still similar, with the 200

W specimen having a somewhat higher ultimate tensile strength. The 150 W and 200 W machined specimens were virtually identical in the strain hardening region and reached almost the same ultimate tensile strengths. One other interesting point from this plot is that the machined specimens appeared to have less ductility than the as-printed ones. This is the opposite of what Everhart et al. [11] observed for AM 17-4 PH stainless steel, although their as-printed specimens did have a lower yield strength. More testing is needed to further examine this effect and the relationship between the measured strengths and cross-sectional area, which Everhart et al. cited as a factor in their tensile tests [11]. Table 4 shows the tensile test results for all Build 1 and 2 specimens.

Table 4. Builds 1 and 2 tensile test results.

Build 1					
Condition	**Laser Power (W)**	**Specimen Location**	**Young's Modulus (GPa)**	**0.2% Offset Yield Strength (MPa)**	**Ultimate Tensile Strength (MPa)**
As Printed	200	2,2	178.1	387.0	550.0
		3,5	175.3	384.7	542.3
		5,3	168.6	380.3	540.2
		6,6	169.1	372.7	526.9
		7,1	155.7	355.4	515.6
		Average, excluding 7,1	*172.8*	*381.2*	*539.9*
		St. Dev., excluding 7,1	*4.679*	*6.297*	*9.606*
Machined	200	1,1	183.9	409.1	567.8
		2,6	172.6	425.2	573.3
		3,3	186.3	417.9	571.0
		5,5	157.0	416.2	570.2
		6,2	167.2	417.1	564.8
		Average	*173.4*	*417.1*	*569.4*
		St. Dev.	*12.09*	*5.724*	*3.245*
Build 2					
Condition	**Laser Power (W)**	**Specimen Location**	**Young's Modulus (GPa)**	**0.2% Offset Yield Strength (MPa)**	**Ultimate Tensile Strength (MPa)**
As Printed	100	5,3	157.3	328.3	428.2
		5,5	154.5	n/a*	201.4*
		6,2	144.1	303.6	361.8
	150	3,3	166.6	373.4	536.0
		1,7	163.4	359.6	395.8
	200	3,5	162.9	366	524.6
		7,1	145.8	328.4	435.8**
		7,7	163.1	358.6	516.5
Machined	100	1,1	140.8	n/a*	270.2*
	150	2,2	173.3	415.7	571.0
		2,6	165.8	414	567.5
	200	6,6	165	410.4	563.5

*The Build 2 specimens from locations 1,1 and 5,5 broke in the grip section
**The Build 2 specimen at 7,1 broke slightly outside of the gauge section.

One interesting result from Build 1 is that the machined specimens all had higher yield and ultimate strengths than the as-printed specimens but had varied Young's modulus results. Two had a Young's modulus above 180 GPa, two fell into the 165-175 GPa range, and another one was at 157 GPa. It is possible that there was extensometer slippage or misalignment during the cycling for this last specimen, especially since there was no apparent change in strength. A change in strength would have indicated that the specimen had a defect. Further tests will help clarify whether this data point is an outlier or within the acceptable range for Young's modulus. Finally, the strength results for the specimen at 7,1 indicate that it was defective in some way. It was thus excluded when calculating the average results and will be analyzed further in terms of its natural frequencies.

In Build 2, as expected, the Young's modulus and strengths of the 100 W laser power specimens were clearly lower than the those of the nominal specimens in Build 1. For the two 100 W specimens that broke in the grip section, the tensile test results are not valid under the ASTM standard. However, from a practical perspective, this result indicates that the parts were defective, especially since the both specimens appeared to fracture at delaminations. This means that the 100 W laser power most likely did not fully bond the melted powder together.

The 150 W and 200 W specimens were difficult to distinguish, aside from the apparently defective specimen at 7,1. Its yield strength was very similar to the 100 W specimen at 5,3. Again, breaking outside of the gauge section invalidates the results under the standard but still indicates a problem with the part.

FEA Modeling

Finite element models can help determine how the modes should vary with material and geometric properties. To identify the sensitivity of the specimen response to changing the stiffness and density of the specimen and build plate, one Baseline Specimen was simulated in ANSYS on a 2 x 2 x 0.5 in. build plate. The downsized model, shown in Fig. 13, eliminates mode splitting that could be present with more specimens on the build plate and focuses the analysis on the response of the specimen. The nominal wrought properties of 304L stainless steel, the specimen material, are given in Table 5 [18]. The material of the build plates was a mild structural steel, with nominal properties used for the modeled build plates in Table 6 [19].

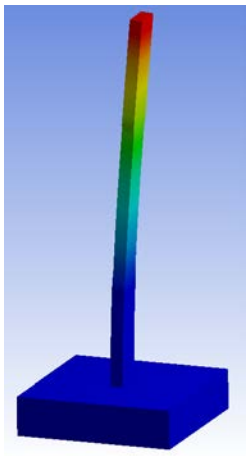

Fig. 13. First mode of Baseline Specimen on miniature build plate.

Table 5. Wrought 304L stainless steel nominal properties.

Density	8.03 g/cc (0.290 lb/in^3)
Young's Modulus	193 GPa (28000 ksi)
Yield Strength (at 0.2% strain)	241 MPa (35000 psi)
Ultimate Tensile Strength	586 MPa (85000 psi)

Table 6. Mild steel (build plate material) nominal properties.

Density	7.85 g/cc (0.284 lb/in^3)
Young's Modulus	210 GPa (30500 ksi)

A frictionless support was applied to the bottom of the build plate, and the model was harmonically excited with a constant force amplitude of 0.0629 N, a value that produced similarly scaled results to the experimental responses. All dimensions and properties aside from those being tested were held at their nominal values. These inputs yielded a nominal frequency of 216.3 Hz for the first mode. Properties were then varied to evaluate the sensitivity of the FRF near the first mode. Based on the equation for a cantilever beam (Eq. 1), the natural frequencies of the specimen should be proportional to the square root of Young's modulus divided by the density. The area moment of inertia I, the length L, and the cross-sectional area A are held constant. The value of the variable α_n is based on what mode shape is being identified.

$$f_n = \frac{\alpha_n}{2\pi L^2}\sqrt{\frac{EI}{\rho A}} \tag{1}$$

In Fig. 14a, Young's modulus of the specimen was varied between 90-110% of the nominal value of 193 GPa. As expected, a positive relationship between Young's modulus and the first natural frequency was found with no significant change in amplitude. In Fig. 14b, the density of the specimen was varied between 90-110% of the nominal value of 8.03 g/cc. Predictably, a negative relationship between specimen density and first natural frequency was observed. As was the case with Young's modulus, there was no significant change in amplitude.

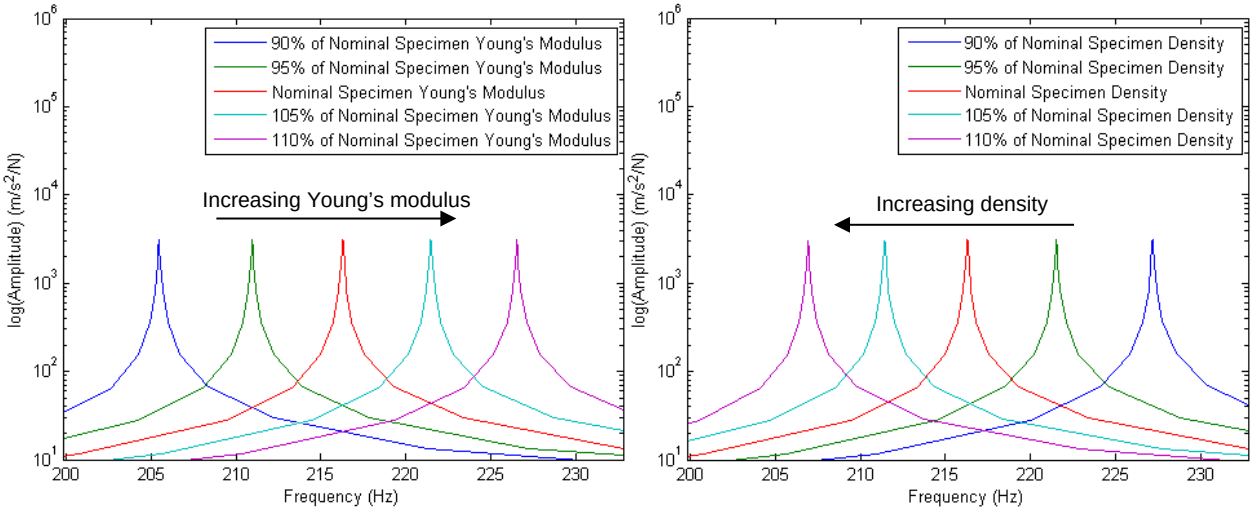

a. FRF with specimen Young's modulus varied. **b. FRF with specimen density varied.**

Fig 14. Relationship between first mode and the specimen Young's modulus, and density.

In Fig. 15a, Young's modulus of the build plate was varied between 90-110% of the nominal value of 210 GPa. Again, a positive relationship was found, but the frequency variation from lowest to highest Young's modulus was less than 1 Hz. No significant change in amplitude was detected. In Fig. 15b, the density of the build plate was varied between 90-110% of the nominal value of 7.85 g/cc. A negative relationship between the build plate density and modal frequency was identified, with a frequency range of about 2 Hz.

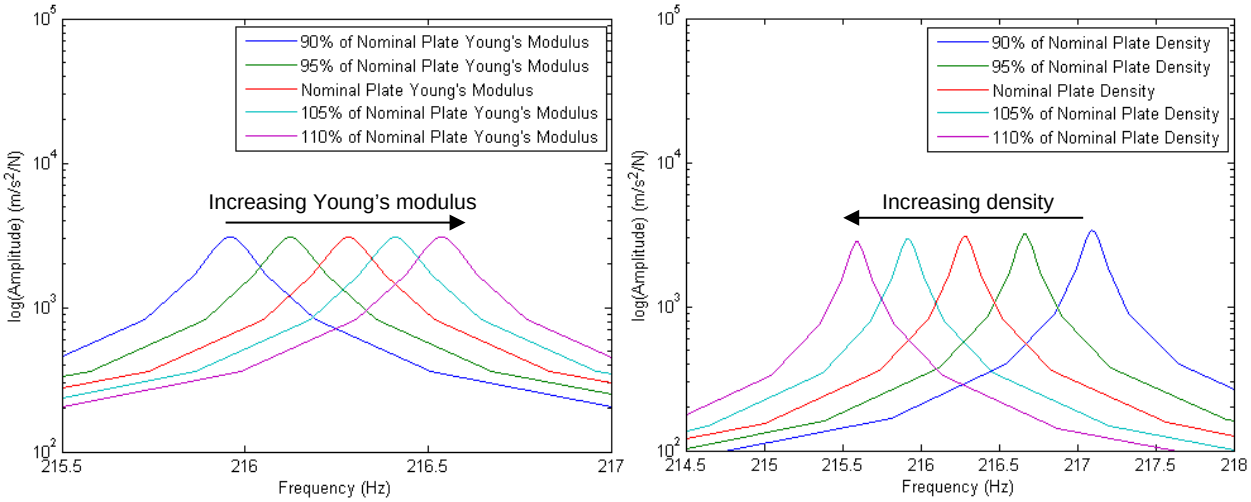

a. FRF with build plate Young's modulus varied. **b. FRF with build plate density varied.**

Fig 15. Relationship between first mode and build plate Young's modulus and density.

In Fig. 16, the thickness of the specimen was varied between 90-110% of the nominal value of 0.15 in. (3.81 mm). The results confirm that the thickness is directly proportional to the frequency, as a 5% change in thickness (0.0075 in.) shifted the first mode by 5% (11.0 Hz). Assuming nominal property values, this means that a baseline specimen would need a tolerance of ±0.0007 inches to be accurate within 1 Hz of the nominal first mode at 216.3 Hz.

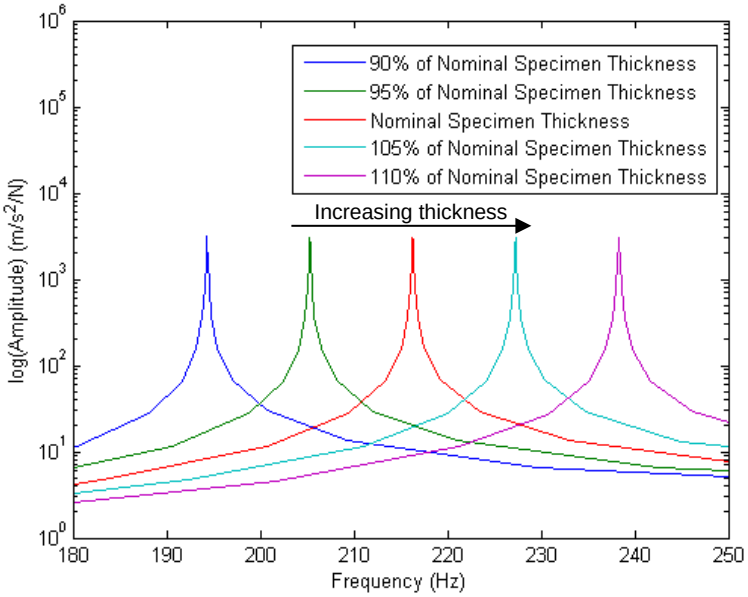

Fig. 16. Relationship between first mode and specimen thickness.

The full Build 1 layout was also modeled in ANSYS with nominal dimensions and a frictionless support on the bottom of the build plate. A harmonic simulation was performed with a constant-amplitude 1.335 N excitation in the *y* direction, which produced FRFs with a similar amplitude to the experimental data. The FRFs measured in the *x* and *y* directions near the first mode are plotted in Fig. 17, along with the experimental data.

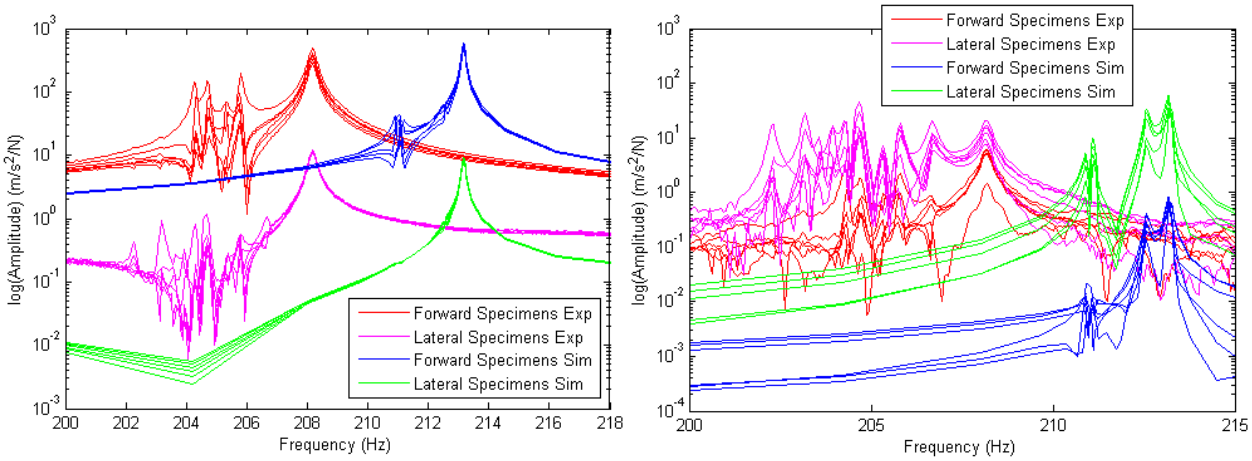

a. FRFs measured in *y* direction. **b. FRFs measured in *x* direction.**

Fig. 17. Experimental and simulated FRFs for Build 1 near mode 1. The simulated FRFs were generated using nominal 304L properties.

The simulated dominant frequency for the forward specimens was at 213.2 Hz while the lateral specimens had an additional dominant frequency at 212.5 Hz. The presence of an *x*-direction response is interesting since the simulated excitation was in the *y* direction. The simulated frictionless support underneath the build plate allowed cross-axis motion similar to that seen on the physical shaker table setup.

The simulated results also displayed the mode-splitting phenomenon seen in the experimental modal testing. Figure 18 shows both the dominant frequency for the forward specimens and one example of mode-splitting at the first mode.

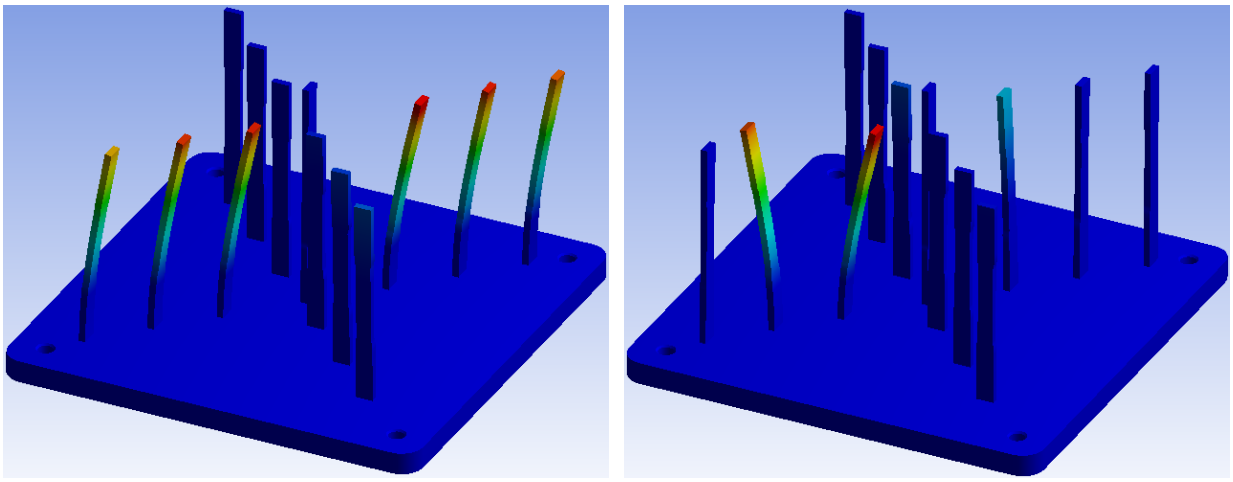

a. Forward specimens at dominant frequency for mode 1. **b. Example of mode-splitting for two specimens.**

Fig. 18. Simulated dominant frequency and mode-splitting at mode 1 for Build 1 specimens.

In all examples of mode-splitting, two specimens vibrated 180º out of phase. At the dominant frequency, all specimens in the same orientation, excluding the Long Specimen, vibrated in phase.

These dominant frequencies using the nominal parameters were about 5 Hz higher than those of the experimental data, and the degenerate modes were more numerous and prominent in the experimental data. Thus, Build 1 was simulated again using the experimental density, cross-sectional dimensions, and Young's modulus of each specimen. The specimens that were not yet tensile tested or density tested were assigned the average Young's modulus and density out of all the Build 1 specimens. The resulting FRFs near the first mode are shown in Fig. 19. The data was split into three main peaks at 221.8, 225.0, and 229.4 Hz due to the material and geometric property variations.

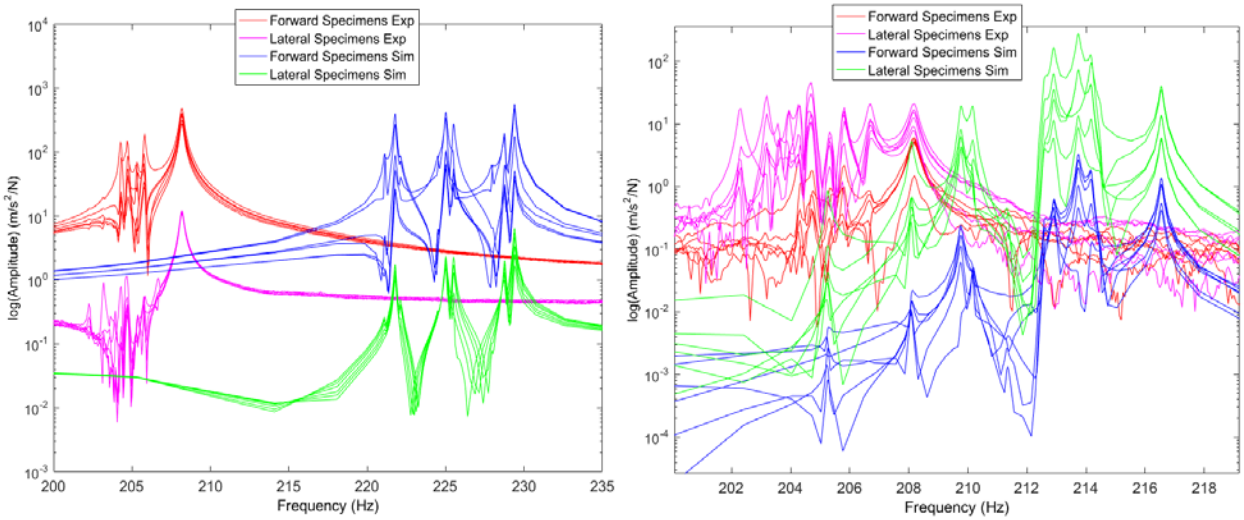

a. Experimental and simulated FRFs measured in the y direction.

b. Experimental and simulated FRFs measured in the *x* direction.

Fig. 19. Experimental and simulated FRFs for Build 1 near mode 1. The simulated FRFs were generated using the experimentally measured cross sectional dimensions, density, and Young's modulus for each specimen.

Compared to the simulations using nominal properties, the *y*-direction data in particular is less similar to the experimental data. Two sets of factors within the model likely contributed to this. First, the behavior of the specimens may not be fully captured through an isotropic model. In the SLM process, uneven cooling may have produced some residual stresses or anisotropic properties, particularly stiffness, in the specimens. Second, the way the boundary condition between the specimens and the plate is modeled can also be refined, as it is currently treated as a bonded joint.

A more significant factor in the discrepancy between simulated and experimental frequencies is perhaps due to uncertainties in the experimentally-measured properties. The most significant uncertainty source is in measuring the cross sectional dimensions. As shown previously, a 5% change in thickness can shift the simulated first natural frequency of an individual Baseline Specimen by about 11 Hz. Without more advanced methods, such as a coordinate measuring machine, it is difficult to quantify the influence of surface roughness and determine the effective cross-sectional area. Errors in these measurements would also have a confounding effect on the Young's modulus and strength measurements from the tensile tests.

Discussion

The density measurement and tensile test results showed that, in general, the Build 1 specimens had fairly similar properties. The one exception to this was the 7,1 specimen, which had a clearly reduced Young's modulus, yield strength, and ultimate tensile strength. These property changes appear to be reflected in the modal analysis. Fig. 20 shows the second mode, measured in the *y* direction. This was the side-to-side bending mode, which was excited in the *y* direction for the lateral specimens, including location 7,1.

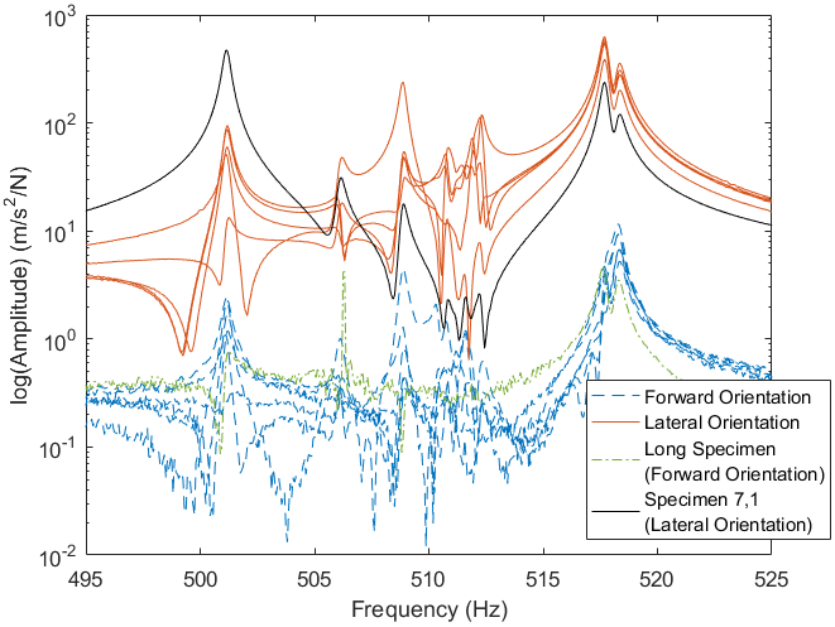

Fig. 20. Second mode of Build 1 specimens, measured in the *y* direction. The FRF for the 7,1 specimen is plotted in black, with the dashed line at the frequency identified by the modal analysis.

While all of the other submodes appeared between 506.1 and 512.3 Hz, with a stronger response at the dominant frequencies near 518 Hz, the strongest response for the 7,1 specimen was at 501.3 Hz, its apparent dominant frequency. The 7,1 specimen also had the lowest identified natural frequency, aside from the Long Specimen, at the first and third modes. Once again, gaining an accurate idea of the effective cross-sectional area and surface roughness of the specimens will help with interpreting these results. Refining the ANSYS model to better reflect the data from a set of parts with nominal properties will also help detect parts like 7,1 that deviate from the nominal behavior. An acceptable range of mechanical properties and natural frequencies can also be determined with more data from nominal parts. This will put modal analysis comparisons between parts on a more quantitative basis, further enabling part validation.

For Build 2, the natural frequencies determined by the modal analysis for each specimen correlated fairly well with the build powers. The main exception to this was again the specimen at 7,1, which was nominally built at 200 W. At the second and third modes, the natural frequencies at 7,1 were significantly below both the 200 W and 150 W specimens. The natural frequency of each specimen at each mode is given in Figures 21-23. Again, no natural frequencies were identified by the modal analysis for the two lateral Scaffold Specimens (locations 2,6 and 7,1) at the first mode.

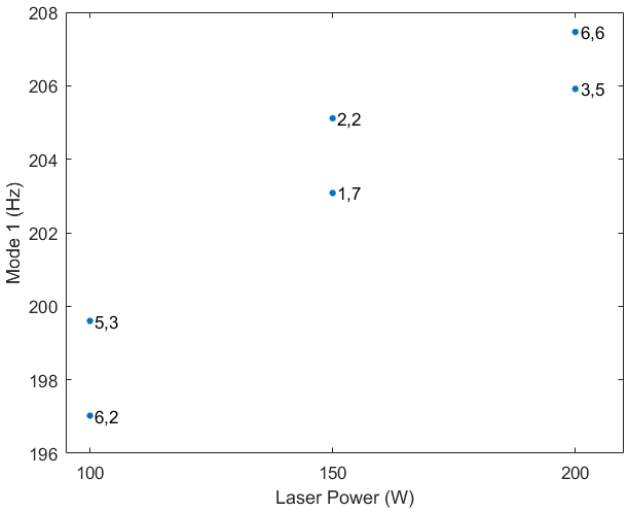

a. Mode 1, Baseline Specimens.

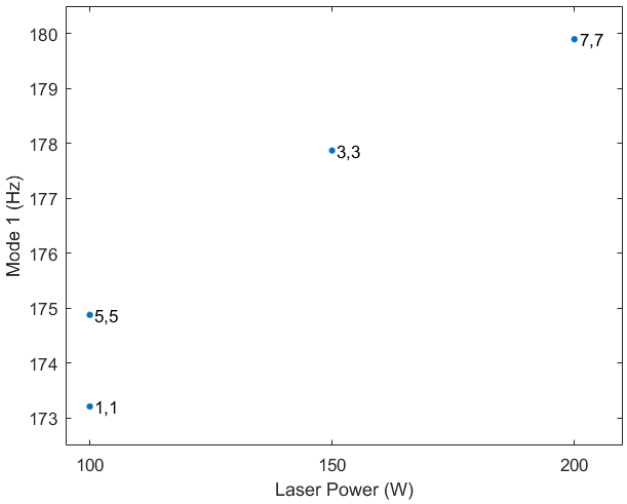

b. Mode 1, Scaffold Specimens (note: no mode identified for Specimens 2,6 and 7,1).

Fig. 21. Mode 1 natural frequency vs. laser power for each Build 2 specimen with location labels.

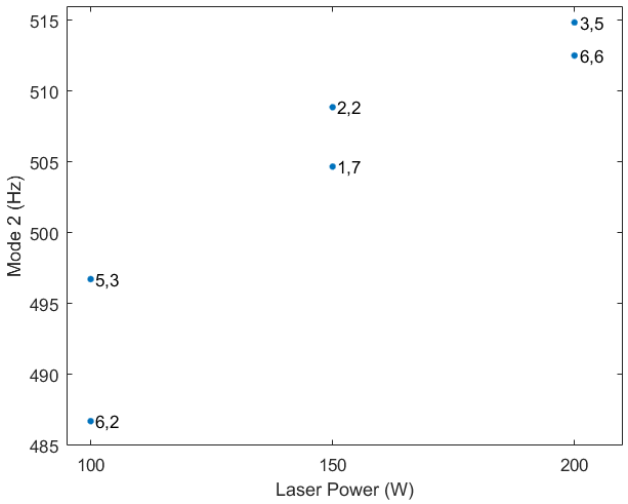

a. Mode 2, Baseline Specimens.

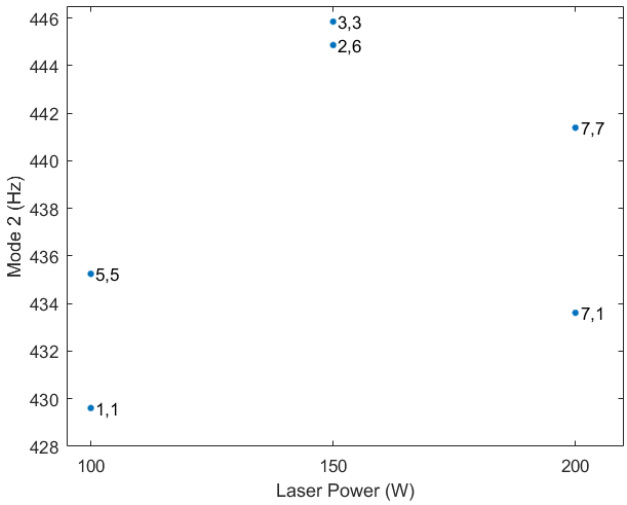

b. Mode 2, Scaffold Specimens.

Fig. 22. Mode 2 natural frequency vs. laser power for each Build 2 specimen with location labels.

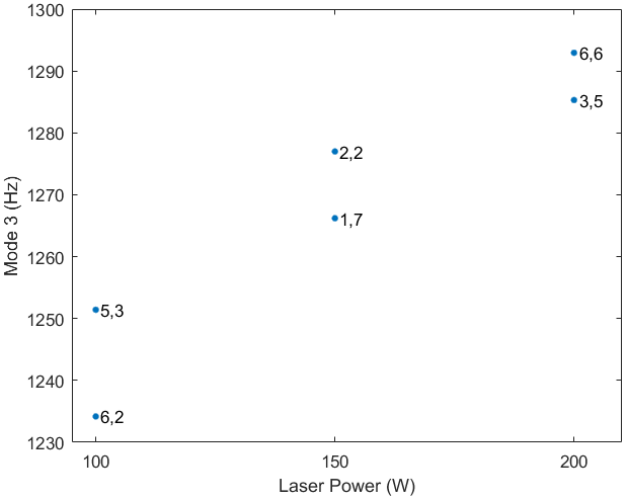

a. Mode 3, Baseline Specimens.

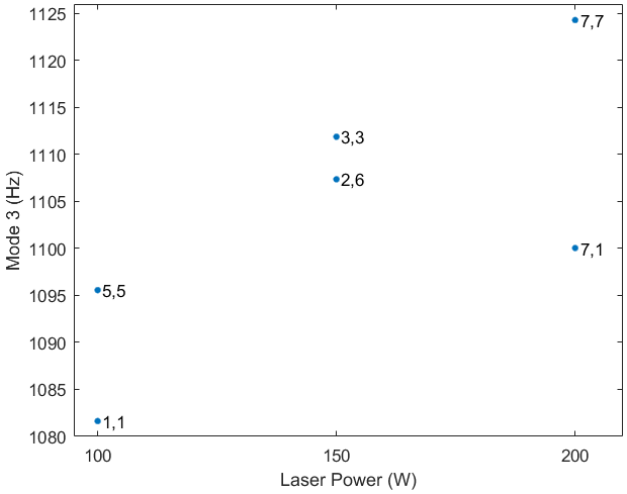

b. Mode 3, Scaffold Specimens.

Fig. 23. Mode 3 natural frequency vs. laser power for each Build 2 specimen with location labels.

Aside from the lower frequencies at 7,1, one other interesting result is in Fig. 22b. At mode 2, the 200 W Scaffold Specimen had a lower natural frequency than the 150 W Scaffold Specimens, although this was reversed for modes 1 and 3. This is most likely due to differences in cross-sectional area, which are further analyzed below. It will also be helpful in the future to include tests with the excitation in the *x* direction to provide more confidence in the natural frequencies identified for each specimen.

To establish modal analysis as a validation technique and to close the loop from build parameters to part performance, it is also important to look at the relationship between a specimen's natural frequencies and its mechanical properties. These relationships are summarized for Build 2 in Table 6. Note the lower natural frequencies and inferior tensile properties of the parts with data in red font (i.e. the 100 W specimens and the specimen at 7,1).

Table 7. Combined modal, density, and tensile test results for Build 2 specimens, with Build 1 average tensile properties, average density, and dominant frequencies at each mode. E/ρ is the Young's modulus to density ratio. Data from parts with the lowest strengths and natural frequencies are in red.

Baseline Specimens									
Laser Power (W)	**Location**	**Young's Modulus (GPa)**	**Yield Strength (MPa)**	**Ultimate Strength (MPa)**	**Density (g/cc)**	**E/ρ (GPa/g/cc)**	**Mode 1 (Hz)**	**Mode 2 (Hz)**	**Mode 3 (Hz)**
100	5,3	157.3	328.3	428.2	7.62	20.6	199.6	496.7	1251.4
	6,2	144.1	303.6	361.8	7.54	19.1	197.0	486.7	1234.2
150	1,7	163.4	359.6	395.8	7.83	20.9	203.1	504.7	1266.2
	2,2*	173.3	415.7	571.0	7.88	22.0	205.1	508.9	1277.0
200	3,5	162.9	366	524.6	7.92	20.7	205.9	514.8	1285.3
	6,6*	165	410.4	563.5	7.86	21.0	207.5	512.5	1292.9
Scaffold Specimens									
Laser Power (W)	**Location**	**Young's Modulus (GPa)**	**Yield Strength (MPa)**	**Ultimate Strength (MPa)**	**Density (g/cc)**	**E/ρ (GPa/g/cc)**	**Mode 1 (Hz)**	**Mode 2 (Hz)**	**Mode 3 (Hz)**
100	1,1*	140.8	n/a	270.2	7.43	18.9	173.2	429.6	1081.6
	5,5	154.5	n/a	201.4	7.58	20.4	174.9	435.2	1095.6
150	2,6*	165.8	414	567.5	7.83	21.2	-	444.9	1107.4
	3,3	166.6	373.4	536.0	7.85	21.2	177.9	445.8	1111.9
200	7,1	145.8	328.4	435.8	7.67	19.0	-	433.6	1100.0
	7,7	163.1	358.6	516.5	7.77	21.0	179.9	441.4	1124.3
Build 1 Average Properties and Dominant Frequencies									
Laser Power (W)	**Specimen Set**	**Young's Modulus (GPa)**	**Yield Strength (MPa)**	**Ultimate Strength (MPa)**	**Density (g/cc)**	**E/ρ (GPa/g/cc)**	**Mode 1 (Hz)**	**Mode 2 (Hz)**	**Mode 3 (Hz)**
200	Build 1 Avg., As Printed	170.4	377.7	536.5	7.89	21.61	206.683, 208.181	517.707, 518.286	(no dominant frequency)
	Build 1 Avg., Machined	173.4	417.1	569.4	7.89	21.99	206.683, 208.181	517.707, 518.286	(no dominant frequency)

*Machined to ASTM E8 standard before tensile testing

The natural frequencies of the specimens should depend on the ratio of Young's modulus to density (E/ρ), so this is a reasonable first metric to consider. For all of the specimens with the lowest natural frequencies, this ratio was 20.6 GPa/g/cc or below. For the rest of the 150 W and 200 W specimens, the ratio was at least 20.7 GPa/g/cc, with the majority above 21.0 GPa/g/cc.

The specimens with the lowest natural frequencies also had by far the lowest yield strengths, following a similar pattern as the E/ρ ratio. The yield strength for these specimens was at most 328.4 MPa, with two of the them breaking at a delamination before a 0.2% offset yield point had been reached. This means that the parts with the worst properties, in terms of Young's modulus, density, and yield strength, were predicted by the modal analysis. This includes the 100 W specimens, which were intentionally built to be inferior, and the 200 W specimen at 7,1, which had an unexpected defect. Further research will likely provide more information on why the specimen at 7,1 was defective in both builds. This location is nearest to both the powder source and the argon source in the build chamber, which may be affecting the specimen's properties.

Finally, as described previously, cross-sectional dimensions are a confounding factor in the correlations between natural frequency and tensile properties. The specimens at 3,3 and 7,7 in Build 2 help show this. The specimen at 3,3 had a higher yield strength and second mode while the one at 7,7 had higher first and third modes. Table 8 shows their cross-sectional dimensions, rounded to the nearest 0.001".

Table 6. Cross-sectional dimensions of the Build 3 specimens at 3,3 and 7,7.

Specimen Location	Width (in.)	Thickness (in.)
3,3	0.357	0.158
7,7	0.360	0.165

While both dimensions are larger at 7,7, the thickness difference is much more significant. Based on Eq. 1, a greater thickness increases the first and third modes while a greater width increases the second mode. Thus, the large difference in thickness likely produced higher first and third modes for this specimen in spite of its lower yield strength. The specimens at 3,3 and 7,7 were also built at 150 W and 200 W, respectively, so in this case, the 150 W part had a higher strength. Further testing will help determine whether parts built at these two powers are in fact significantly different.

Conclusion

Overall, modal analysis was shown to be a promising validation technique for metal AM parts. In Build 2, the modal analysis showed a clearly lower set of natural frequencies for the specimens build at 100 W laser power. It also measured a lower set of natural frequencies for the specimen at 7,1 in both builds. These decreases in natural frequency corresponded to decreases in yield strength and stiffness, showing that the modal analysis could effectively reject these parts. The 100 W parts all broke at apparent delaminations, which would decrease the stiffness of the parts, while efforts are ongoing to determine the cause of the weakened parts at 7,1.

Future work will be focused in three main areas. First, more accurate cross-sectional dimension measurements are needed to determine the effective dimensions for the modal and tensile tests. One possible path towards this objective is CT scanning cross sections of several of the

specimens to characterize surface roughness. Second, the ANSYS models need to be refined to more closely match experimental data from nominal, undamaged specimens. The cross sectional dimensions will help significantly with this. Other aspects of the model to consider include the boundary conditions between the specimen and the plate and anisotropy arising from the build process. A more accurate model can help characterize changes in the modal response that occur due to certain defects, providing a degree of defect prognosis. Finally, the entire testing process can be repeated for specimens with different sets of varied build parameters. This is important in order to establish a detection threshold for the technique, which is necessary prior to implementation for real parts.

Acknowledgments

This work has been funded by Honeywell Federal Manufacturing & Technologies under Contract No. DE-NA0002839 with the U.S. Department of Energy. The United States Government retains and the publisher, by accepting the article for publication, acknowledges that the United States Government retains a nonexclusive, paid up, irrevocable, world-wide license to publish or reproduce the published form of this manuscript, or allow others to do so, for the United States Government purposes. This work contains a patent pending technique, U.S. Patent Application Serial No. 14/941,258.

References

[1] Frazier, W.E., 2014, "Metal Additive Manufacturing: A Review," JMEP, **23**(6), pp. 1917-1928.

[2] Nannan, G. and Leu, M.C., 2013, "Additive Manufacturing: Technology, Applications, and Research Needs," Front. Mech. Eng., **8**(3), pp. 215-243.

[3] Niendorf, T. and Brenne, F., 2013, "Steel Showing Twinning-Induced Plasticity Processed by Selective Laser Melting – An Additively Manufactured High-Performance Material," Mater. Charac., **85**(2013), pp. 57-63.

[4] Sharratt, B.M., 2015, "Non-Destructive Techniques and Technologies for Qualification of Additive Manufactured Parts and Processes: A Literature Review," Sharratt Research and Consulting Inc., Victoria, BC, Canada.

[5] Ziolkowski, G., Chlebus, E., Szymczyk, P. and Kurzac, J., 2014, "Application of X-Ray CT Method for Discontinuity and Porosity Detection in 316L Stainless Steel Parts Produced with SLM Technology," Arch. Civ. Mech. Eng., **14**(2014), pp. 608-614.

[6] Léonard, F., Tammas-Williams, S., Prangnell, P.B., Todd, I. and Withers, P.J., 2012, "Assessment by X-Ray CT of the Effects of Geometry and Build Direction on Defects in Titanium ALM Parts," *2nd Conference on Industrial Computed Tomography (ICT)*, Wels, Austria, pp. 85-93.

[7] Tammas-Williams, S., Zhao, H., Léonard, F., Derguti, F., Todd, I. and Prangnell, P.B., 2015, "XCT Analysis of the Influence of Melt Strategies on Defect Population in Ti-6Al-4V Components Manufactured by Selective Electron Beam Melting," Mater. Charac., **102**(2015), pp. 47-61.

[8] Slotwinski, J.A., Garboczi, E.J. and Hebenstreit, K.M., 2014, "Porosity Measurements and Analysis for Metal Additive Manufacturing Process Control," Journal of Research of NIST, **119**(2014), pp. 494-528.

[9] Karthik, N.V., Gu, H., Pal, D., Starr, T. and Stucker, B., 2013, "High Frequency Ultrasonic Non Destructive Evaluation of Additively Manufactured Components," *24th International Solid Freeform Fabrication Symposium*, Austin, TX, pp. 311-325.

[10] Wang, Z., Palmer, T.A. and Beese, A.M., 2016, "Effect of Processing Parameters on Microstructure and Tensile Properties of Austenitic Stainless Steel 304L Made by Directed Energy Deposition Additive Manufacturing," Acta Mater., **110**(2016), pp. 226-235.

[11] Everhart, W., Sawyer, E., Neidt, T., Dinardo, J. and Brown, B., 2016, "The Effect of Surface Finish on Tensile Behavior of Additively Manufactured Tensile Bars," J. Mater. Sci., **51**(8), pp. 3836-3845.

[12] Hearn, G. and Testa, R.B., "Modal analysis for damage detection in structures," Journal of Structural Engineering **117**(10), pp. 3042-3063.

[13] Doebling, S.W., Farrar, C.R. and Prime, M.B., "A Summary Review of Vibration-Based Damage Identification Methods," The Shock and Vibration Digest **30**(2), pp. 91-105.

[14] Stultz, G.R., Bono, R.W. and Schiefer, M.I., 2005, "Fundamentals of Resonant Acoustic Method NDT," The Modal Shop Inc., Cincinnati.

[15] Lai, C., Sun, X., Dasch, C., Harmon, G. and Jones, M., "Quantify Resonance Inspection with Finite Element-Based Modal Analysis," J. Vib. Acoust. **133**(3), p. 031004.

[16] Schoneman, J.D. and Allen, M.S., 2016, "Modal Test and Parameter Updating of Metal Laser Sintered Components," *Topics in Modal Analysis & Testing: Proceedings of the 34th IMAC, A Conference and Exposition on Structural Dynamics 2016*, **10**, Orlando, pp. 223-233.

[17] ASTM, 2015, "Standard Test Methods for Tension Testing of Metallic Materials," ASTM E8/E8M-15a.

[18] AK Steel, 2016, "AK Steel 304L Austenitic Stainless Steel," from http://www.matweb.com/search/datasheet.aspx?matguid=8379d9f31c8243acbf350273660ea83e.

[19] Geocentrix Ltd., 2004, "Structural Steels," from http://www.geocentrix.co.uk/help/content/items/steels/structural_steels.htm.

[20] ASTM, 2013, “Standard Test Method for Density of Powder Metallurgy (PM) Materials Containing Less Than Two Percent Porosity,” ASTM B311-13.

[21] ASTM, 2010, “Standard Test Method for Young’s Modulus, Tangent Modulus, and Chord Modulus,” ASTM E111-04(2010).